

## Sub-nm Curvature Unlocks Exceptional Inherent Flexoelectricity in Graphene

Sathvik Ajay Iyengar<sup>1</sup>, James G. McHugh<sup>2</sup>, Jonathan P. Salvage<sup>3</sup>, Robert Vajtai<sup>1</sup>, Alan Dalton<sup>4\*</sup>, Manoj Tripathi<sup>4\*</sup>, Pulickel M. Ajayan<sup>1\*</sup>, Vincent Meunier<sup>5\*</sup>

<sup>1</sup> *Department of Materials Science and NanoEngineering, Rice University; Houston, TX, 77005 USA*

<sup>2</sup> *National Graphene Institute, University of Manchester, Booth St. E., Manchester, M13 9PL, United Kingdom*

<sup>3</sup> *School of Pharmacy and Biomolecular Science, University of Brighton, Brighton BN2 4GJ, U.K*

<sup>4</sup> *Department of Physics and Astronomy, School of Mathematical and Physical Sciences, University of Sussex; Brighton BN1 9QH, United Kingdom*

<sup>5</sup> *Department of Engineering Science and Mechanics, Pennsylvania State University; University Park, PA, 16802, USA*

\*Corresponding author. Email: Alan Dalton [A.B.Dalton@sussex.ac.uk](mailto:A.B.Dalton@sussex.ac.uk), M.Tripathi@sussex.ac.uk, [ajayan@rice.edu](mailto:ajayan@rice.edu), [vincent.meunier@psu.edu](mailto:vincent.meunier@psu.edu)

### Abstract

Flexoelectricity arises from strain-gradient-induced polarization and is particularly pronounced in two-dimensional (2D) materials due to their exceptional mechanical flexibility and sensitivity to structural deformations. This phenomenon approaches its fundamental limit in highly curved nanostructures, where extreme charge redistribution and electrostatic modulation result in macroscopic manifestations, such as electronic band offsets, that can be directly measured. Here, we present the first direct experimental and theoretical demonstration of giant intrinsic flexoelectricity in graphene nanowrinkles. These nanowrinkles feature a consistent radius of curvature of  $\sim 5 \text{ \AA}$  atop a flat MoS<sub>2</sub> substrate, where strain gradients, mapped by sub-micron Raman spectroscopy, emerge from mismatched elastic properties between graphene and MoS<sub>2</sub>. Conductive atomic force microscopy (c-AFM) reveals consistent and reproducible flexoelectric currents over large-area, dense nanowrinkle networks. The observed asymmetric electromechanical behavior, characterized by a threshold potential ( $\Phi_{th}$ ) of  $\sim 1 \text{ V}$ , suggests the presence of an intrinsic energy barrier to overcome to activate a flexoelectric current. This threshold likely arises from combined band alignment effects and strain-induced polarization barriers, which modulate carrier transport at the wrinkle apex. Notably, this behavior aligns with our theoretical band offset predictions ( $\sim 1.2 \text{ V}$ ), further supporting the role of flexoelectric dipoles in modifying local electrostatic potential. To our knowledge, this represents the strongest manifestations of flexoelectricity in nanostructures with intrinsic polarization densities  $10^5$ - $10^7$  times greater than meso/micro counterparts yielding  $P_{th} \sim 4 \text{ C/m}^2$ ,  $P_{exp} \sim 1 \text{ C/m}^2$ . This work establishes graphene nanowrinkles as a model system for exploring giant nanoscale flexoelectric effects and highlights their potential for strain-engineered nanoscale electronic and electromechanical devices.

## Main

Flexoelectricity, the coupling between strain gradients and polarization, is a universal electromechanical phenomenon that occurs even in centrosymmetric materials (1–3). Kalinin and Meunier (4) first theorized in 2008 that mechanical deformations in 2D membranes, such as wrinkles or localized curvature, could generate strain gradients and induce polarization (5, 6). Unlike piezoelectricity, which is restricted to non-centrosymmetric materials, flexoelectricity arises in any material subjected to non-uniform strain, making it particularly relevant to low-dimensional systems such as two-dimensional (2D) materials (4).

Theoretical studies have predicted significant flexoelectric behavior in graphene and transition metal dichalcogenides (TMDs) due to their high mechanical flexibility and strain-induced dipole formation (7, 8), yet direct experimental confirmation, particularly in carbon nanomaterials, remains limited. While flexoelectricity is ubiquitous, it is often obscured by dominant piezoelectric interactions or weakened by depolarization effects caused by structural imperfections and chemical additives—especially in systems with only small to moderate curvatures ( $< 10^3 \text{ m}^{-1}$ ). Fully tapping into the potential of flexoelectricity requires the development of materials that are structurally coherent, defect-free, centrosymmetric, and characterized by pronounced curvature at the nanoscale.

Van der Waals (vdW) heterostructures provide a unique platform for investigating strain-gradient-driven effects, as their weak interlayer coupling enables controlled mechanical deformations (9). Graphene, with its exceptional mechanical flexibility, offers an opportunity to probe the fundamental limit of flexoelectricity, where extreme curvature and strain confinement lead to pronounced polarization effects. In contrast to bulk materials, where competing electromechanical phenomena obscure flexoelectricity (10), 2D systems allow for direct investigation of strain-gradient-induced charge redistribution at the nanoscale. A distinct advantage of 2D–2D vdW heterostructures over 2D–3D systems is the comparable contribution of each 2D layer in influencing the heterointerface dynamics.

Despite their promise, experimental studies of flexoelectricity in 2D systems have faced significant challenges. Centrosymmetric semiconductors such as Si and  $\text{TiO}_2$  have demonstrated strain-induced polarization, but substrate interactions and indirect measurement complexities often obscure intrinsic flexoelectricity (11, 12). Similarly, reports on indium selenide and indium oxide nanosheets suggest flexoelectric responses, yet isolating pure flexoelectric contributions proved difficult due to competing piezoelectric effects (13, 14). Most importantly, experimental demonstrations of the flexoelectric effect thus far are under strain fields ( $\sim 10^6 \text{ m}^{-1}$ ) (still far from giant fields  $\sim 10^{10} \text{ m}^{-1}$ ) and are yet extrinsic and short-lived—caused by massive indentation forces applied by cantilever probes (15, 16).

Recent work has demonstrated a flexo-photovoltaic effect in  $\text{MoS}_2$  using hybrid heterostructures incorporating  $\text{VO}_2$  phase-change materials, where strain gradients drive polarization (17). However, phase transitions and complex hybrid systems limit reproducibility and scalability. In contrast, graphene, with its purely centrosymmetric lattice, extreme mechanical flexibility, and quasi-pristine structure (minimizing dipoles from dopants and defects), provides a simpler yet more promising system for isolating and amplifying flexoelectric effects at the nanoscale (18).

Here, we use self-assembled graphene nanowrinkles (NWs) as a model system to explore giant flexoelectricity, where extreme nanoscale curvature maximizes strain gradients and has only been theorized till date (19). By leveraging a flat  $\text{MoS}_2$  substrate to drive wrinkle formation through

mechanical mismatch, we achieve a highly controlled, large-area realization of flexoelectricity without extrinsic phase transitions or hybrid material complications. Conductive atomic force microscopy (c-AFM) reveals asymmetric electromechanical responses within highly curved regions, confirming flexoelectricity in graphene. This study establishes a scalable, reproducible approach to strain-engineered electronic and electromechanical devices based on pure flexoelectric behavior in carbon nanomaterials.

This macroscopically detectable manifestation of flexoelectricity originates from confined flexion within self-assembled graphene NWs, where strain gradients induce strong polarization effects. Unlike piezoelectricity (**Fig. 1A (i)**), which arises from compressing a non-centrosymmetric crystal, flexoelectricity (**Fig. 1A (ii)**) occurs in centrosymmetric materials under strain gradients. In graphene NWs, the giant flexoelectric response (**Fig. 1A (iii)**) is a direct consequence of extreme curvature-driven strain gradients, pushing flexoelectricity to its upper limit within a purely carbon-based system. The formation of these NWs is dictated by the mechanical mismatch between graphene and MoS<sub>2</sub>, where the latter promotes wrinkle formation more effectively than silica due to its distinct elastic properties. The incommensurate graphene-MoS<sub>2</sub> interface, resulting from their differing lattice constants (0.31 nm for MoS<sub>2</sub> and 0.24 nm for graphene), along with differences in Poisson's ratios, drives spontaneous buckling under tension. Additionally, the mismatched Young's modulus facilitates self-assembly shear-slide, further enhancing wrinkle formation (**Fig. 1B**). This is consistent with the 'standing-collapsed' architecture inherent to graphene under extreme strain fields (i.e., closed loops) as we previously demonstrated experimentally by transmission electron microscopy and confirmed by DFT simulations (20), and also confirmed experimentally by AFM measurements in this study, see **Fig. S1**.

A key factor in this morphology is the bending modulus difference: Graphene, with a modulus ( $1.0 \pm 0.1$  TPa) (21) one order higher than MoS<sub>2</sub> ( $\sim 270 \pm 100$  GPa) (22), can wrinkle under tensile strain, to maximize interaction with the substrate. The energy cost of bending is further offset by vdW interaction between the vertical walls of the NW. The lower interfacial shear force between graphene and MoS<sub>2</sub> compared to graphene and silica enables graphene to slide and form pronounced wrinkles, as revealed by friction force mapping (**Fig. S2**), which shows a threefold friction difference between Gr/MoS<sub>2</sub> and Gr/silica. AFM and SEM measurements indicate that graphene NWs on MoS<sub>2</sub> reach heights of 6–8 nm, with a roughness ( $R_q = 2.78$  nm,  $R_a = 1.73$  nm) nearly six times higher than on silica ( $R_q = 0.48$  nm,  $R_a = 0.28$  nm) (extracted from data in **Fig. 2A**). Unlike traditional wrinkle formation in CVD graphene due to thermal expansion mismatch, the MoS<sub>2</sub> substrate enhances wrinkle height and density in physically deposited graphene (more details in **Fig. S3**). Molecular dynamics simulations indicate this assembly is extremely rapid: small wrinkles spontaneously nucleate for local uniaxial strains  $\epsilon_x > 0.02$  and subsequently agglomerate by sliding across the MoS<sub>2</sub> within a 0.1 ns time scale. (**Fig. 1C**).

The resulting NWs form a curvature-driven ripple, exhibiting a net polarization leading to the relationship:

$$P = f(c_1 + c_2) \quad (1)$$

where  $P$  is the induced polarization,  $f$  is the flexoelectric constant, and  $c_1$  and  $c_2$  are the principal Gaussian curvatures on the surface. Here, the first Gaussian curvature in the plane of the graphene sheet (along the ripple),  $c_1$ , is  $\sim 0$ , and the second Gaussian curvature in the perpendicular direction,  $c_2 = 1/R$ , where  $R$  is

the radius of curvature, when we approximate the tip of the NW as roughly circular, as depicted in **Fig. 1D**) therefore:

$$P = f/R, \quad (2)$$

showing that the polarization effect is strongest in materials with a large flexoelectric constant and a small local radius of curvature. In bulk perovskites, for example,  $f$  is typically on the order of  $\sim$  nC/m (23), whereas in 2D systems, values can vary widely depending on material properties and strain conditions. For graphene, DFT predicts  $f \sim 2$  nC/m (4). While direct measurements of  $f$  in graphene are challenging, our experimental results and observed polarization response closely match DFT predictions, confirming the estimated value of  $f$ .

What distinguishes nanomaterials is not necessarily a large flexoelectric constant—no greater than that found in biological membranes (24)—but rather the ability to achieve nanometer-scale radii of curvature. In carbon nanostructures, a reasonable lower limit for curvature is the radius  $R \sim 3.4 \text{ \AA}$  as seen in  $C_{60}$  fullerenes or (5,5) and (9,0) nanotubes. However, despite their high curvature, these closed structures do not exhibit net polarization due to their symmetric assembly—each local curvature-induced dipole, while potentially large (25) is canceled by an opposing antiparallel dipole. In contrast, the NWs considered here exhibit a local curvature corresponding to an estimated radius of  $\sim 5 \text{ \AA}$  (20), approaching the lower limit, yet without a canceling effect. This unique structural asymmetry allows for a net flexoelectric response, distinguishing NWs from other carbon-based nanostructures.

It follows that the emerging polarization can lead to measurable effects on the electronic properties. For instance, the pronounced work function shift observed in our study underscores the dominant role of the flexoelectric effect over any substrate-driven influence. This is evident in the significant work function shift as measured by Kelvin Probe Force Microscopy (KPFM) (**Fig. 1E-F**), where graphene NWs ( $\sim 4.9$  eV) exhibit values closer to pure silica ( $\sim 4.97 \pm 0.28$  eV) than unflexed graphene on  $\text{MoS}_2$  ( $\sim 5.27 \pm 0.1$  eV) or silica ( $\sim 5.17 \pm 0.1$  eV). If  $\text{MoS}_2$  were to influence the electronic structure through substrate-driven work function shifts, this effect would be uniform across the entire material rather than localized to NW. Instead, the observed charge redistribution is highly confined to flexed regions, demonstrating that the flexoelectric effect ( $\delta \sim 0.4$  eV) is far stronger than any global substrate-mediated doping or screening ( $\delta \sim 0.1$  eV). The stark deviation of NW work function values from those of unflexed graphene further confirms that substrate interactions play a negligible role in modulating local charge distribution. Instead, the observed shift originates from flexoelectric-induced polarization. This tunability of the work function via strain gradients opens potential applications in graphene-based energy harvesting, tunable Schottky junctions, and strain-gated electronic devices, where precise control over electronic properties is critical.

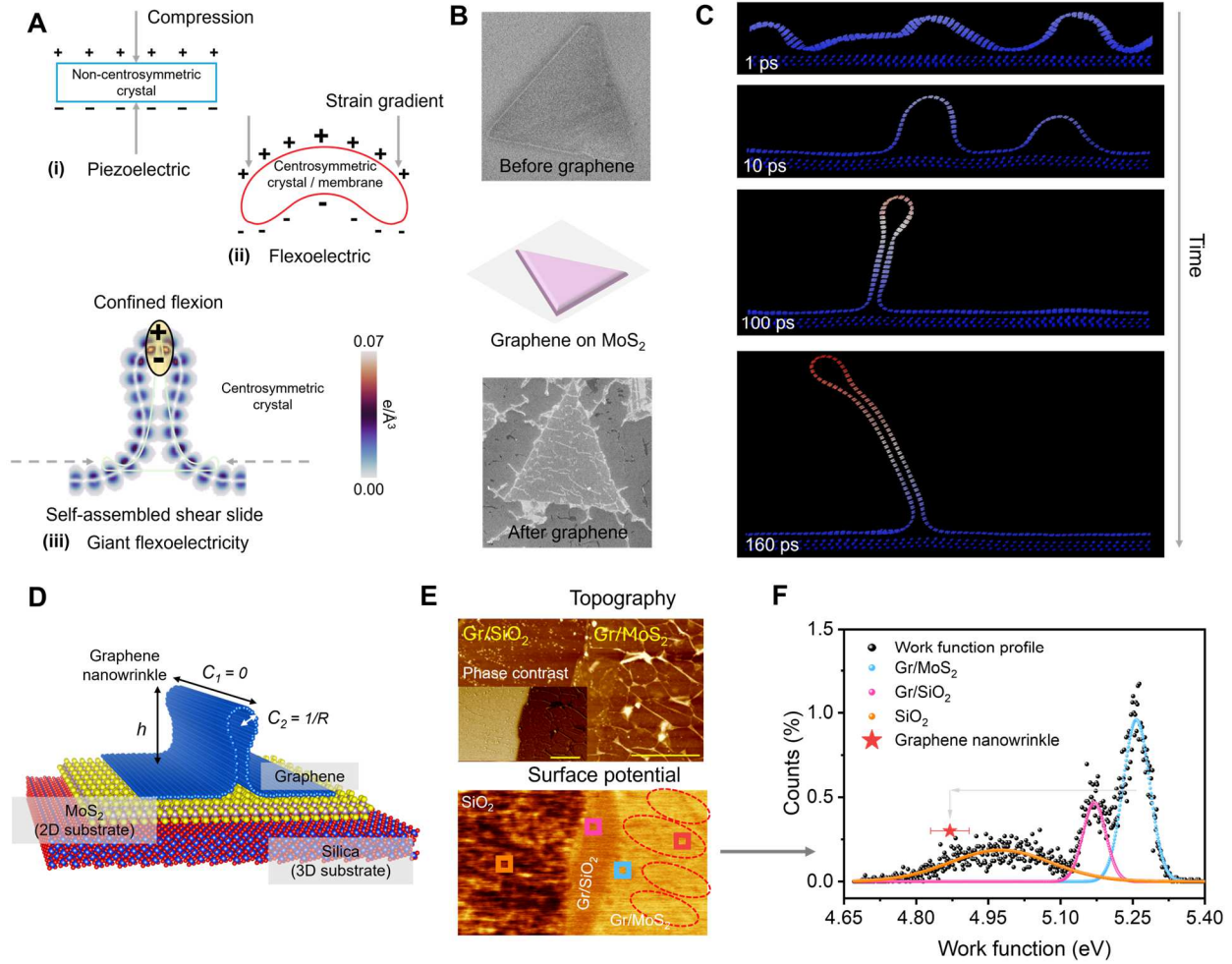


**Figure 1. A platform for giant flexoelectricity.** (A) Schematic illustration comparing (i) piezoelectricity, (ii) flexoelectricity, and (iii) giant flexoelectricity based on crystal centrosymmetry, methods of compression/strain, mechanisms of relaxation, and curvature. The charge density in (iii) is obtained by DFT and shows the density in a 2 eV window below the Fermi energy. (B) Scanning electron microscopy (SEM) micrographs of a flat MoS<sub>2</sub> substrate before and after the transfer of monolayer graphene and subsequent NW self-assembly. (C) Molecular dynamics simulations depicting the time evolution of NW self-assembly at  $T = 100$  K. Smaller wrinkles spontaneously nucleate under compressive strains  $\epsilon_x > 0.02$ , and rapidly combine into large, standing collapsed wrinkles within a 0.16 ns time scale. (D) Schematic representation showing the carbon NW (blue) on MoS<sub>2</sub> (yellow/grey), on top of SiO<sub>2</sub> substrate (red and dark blue). The schematics show the Gaussian curvatures in the NW, utilized to establish the giant flexoelectric formalism. (E) Atomic force microscopy (AFM) is used for topography and phase contrast, with corresponding Kelvin probe force microscopy (KPFM) measuring surface potential across different substrate regimes. (F) Work function distribution across surfaces, highlighting the significant shifts observed in graphene NW compared to expected values. All scale bars are 1  $\mu$ m.

From experiment and theory, we establish that the flexoelectric effect is also independent of the NW height, making it a reliable method for creating high-density wrinkle networks that behave identically. This also highlights the central role of the localized curvature at the top of the wrinkle, further confirming that the observed phenomena are indeed due to flexoelectricity. If we consider such a network (**Fig. 2A**),

with wrinkles of varying heights, when a fixed bias (2 V) is applied (**Fig. 2B**), all NWs yield a similar value of flexoelectric current ( $\sim 67$  pA) (**Fig. 2C**). The presence of the polarization induced by the NW leads to a significant change in work function in the vicinity of the wrinkles compared to a flat graphene sheet, as predicted by DFT (**Fig. 2D**). The presence of flat graphene areas along with the NW, leads to a band offset in the type I heterojunction (**Fig. 2E**).

In addition, to further investigate variations based on NW height, we performed DFT calculations for three different cases, now referred to as NW1 ( $h = 15.64$  Å), NW2 ( $h = 27.54$  Å), and NW3 ( $h = 39.99$  Å) (see **SI methods, Fig. S4**). The results show that the flexoelectric effect is preserved regardless of height (**Fig. S5**), confirming that the curvature at the NW tip is the driving force behind the observed phenomena. Further characterization of the electronic properties of the NWs in **Figs. 2F–G** reveals that the field induced by charge reorganization in response to an external field (depolarization) highlights the key role of the NW apex (NW1 and 2 in **Fig. S6**). Within the the same system, the role of curvature is clearly dominant—and the only influencing factor—not the height of the feature, as shown by measurements across different structures in **Fig. S7**.

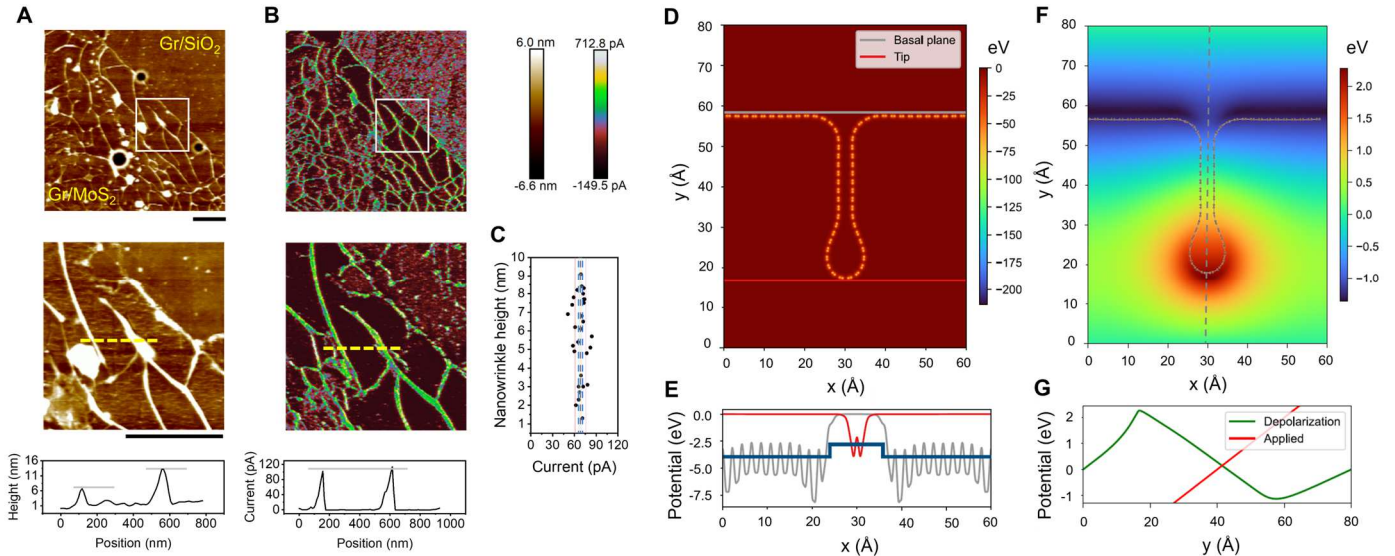


**Figure 2. Large-area, uniform, and highly polarized giant flexoelectricity.** (A) Atomic force microscopy (AFM) and (B) corresponding conductive AFM characterization of the topology and current distribution of graphene NW. Interestingly, only the NWs exhibit a higher baseline current, which is independent of NW height (i.e., independent of height  $h$ ), as shown in (C). (D) Electrostatic potential map of a NW with potential extracted at the tip and basal plane, as shown in (E). (E) also shows the macroscopic average potential (blue), showing that the flexoelectric polarization yields a reduction of the work function at the wrinkle tip and the ensuing band alignment. (F) Calculated depolarization field for NW, with contrasting features between the applied and depolarization fields illustrated in (G), showing that no net electric field is present in the material. All scale bars are 1  $\mu\text{m}$ .

Interestingly, flexoelectric strain is predominantly tensile, providing key insight into the asymmetric electronic features discussed later. For a typical high-density region of graphene nanowrinkles (NWs) (**Fig. 3A**), we observe up to 0.05% tensile strain, as calculated from Raman maps (**Fig. 3B**). These values, however, likely underestimate the actual strain due to the averaging effect of Raman mapping, which has

a spot size of  $\sim 300$  nm (26). Graphene nanostructures exhibit a range of morphologies, including wrinkles, folds, and bubbles, all of which fall within a similar strain range. Our previous work reports strain values of  $(0.03 \pm 0.01)\%$  for graphene bubbles and  $(0.04 \pm 0.01)\%$  for transitional folded wrinkles (27). More broadly, curvature-induced strain in 2D materials typically falls within the  $10^{-2}$  range (28). Despite these comparable strain values, NWs occupy the upper limit of this range and exhibit a unique structural character. Unlike bubbles or folds, NWs possess extremely low curvature yet break symmetry in a way that induces polarization. This distinction is crucial when juxtaposed with Raman data (**Fig. S8**), which shows little to no D-band signal, ruling out defect-driven effects. Strain field calculations based on bond-length fluctuations reveal significant buckling under flexion near the NW bud of curvature  $c_2$ . **Fig. 3C** presents strain gradient values for a DFT-relaxed NW, mapping bond-length variations in the vicinity and away from the NW (NW1 and NW2 in **Fig. S9**).

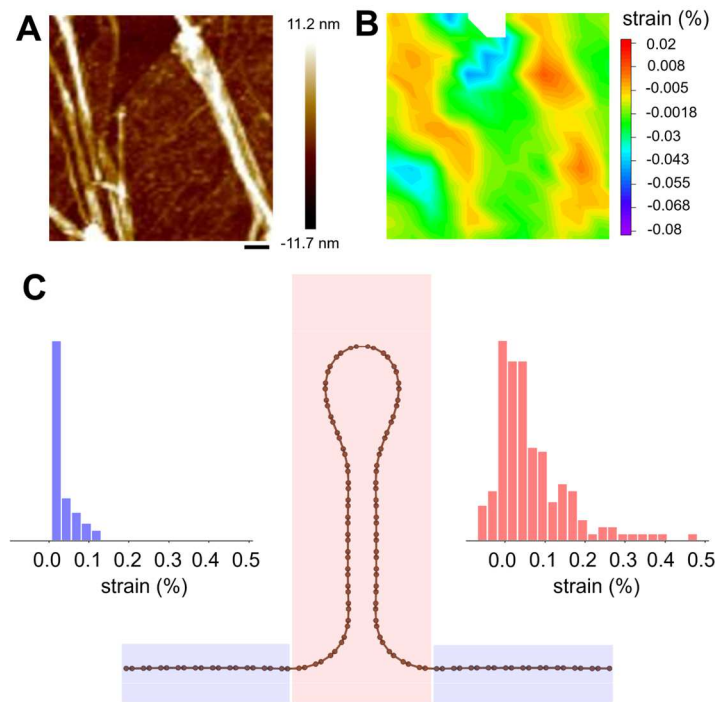


**Figure 3. Strain correlated studies.** (A) AFM topology and corresponding (B) Strain map obtained from Raman spectroscopy maps (C) Histogram of calculated lattice strain across a graphene NW. All scale bars are 1  $\mu\text{m}$ .

To further investigate the flexoelectric response, we performed measurements under varying bias conditions (**Fig. 4A**). As observed previously, and confirmed by our DFT calculations, the effect depends on the applied bias and remains uniform for a given bias, regardless of NW height, resulting in large-area coverage and reproducibility, as seen in **Fig. 4B**. Dipole moments calculated for these systems were found to be  $0.0261 e \text{ \AA}$  (0.125 D),  $0.0223 e \text{ \AA}$  (0.107 D), and  $0.0297 e \text{ \AA}$  (0.143 D), respectively (see **Fig. S10**). This shows minimal variation across various sizes of NWs. **Fig. 4C** analyzes four specific NWs, looping the same spatial resolution across different voltages, and reveals a clear asymmetry in response when probing low and negative biases. In this bias regime, a threshold voltage ( $\Phi_{th}$ ) of  $\sim 1.01$  V is observed (**Fig. 4D**), corresponding to a barrier potential that must be overcome, consistent with the flexoelectric

dipole induced in the NW. These findings validate our theoretical predictions of band offset value ( $\sim 1.2$  V) and demonstrate the influence of strain gradients on electron distribution and electrostatic properties within confined 2D volumes.

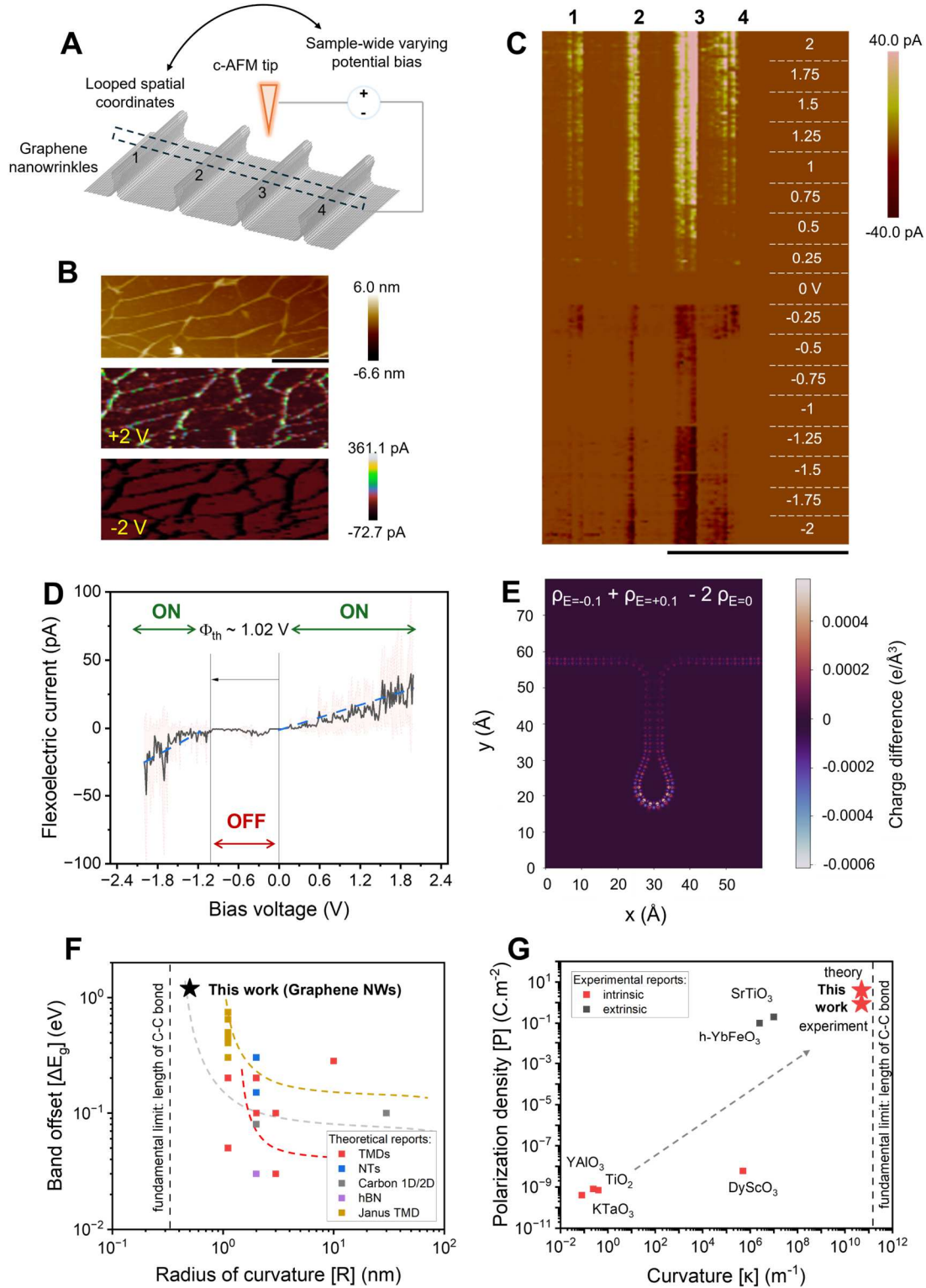




**Figure 4. Potential bias dynamics of flexoelectrics.** (A) Conductive Atomic Force Microscopy (CAFM) measurement setup to study flexoelectric response in graphene NW (B) spatially-resolved CAFM data under fixed opposite biases show asymmetry in current response (C) Bias voltage-dependent data where each ‘strip’ consists of a repeated area over the sample under a different potential. Numbers indicate the position of 4 NW. At zero bias, the NW’s flexoelectric signatures are not observed and come to being when bias is applied. (D) Flexoelectric current measurements were collected specifically on NW and averaged across a bias range. (E) Asymmetry in electrostatic response obtained by computing charge density difference between opposite and equal magnitude potential fields. The presence of flexoelectric polarization is responsible for the asymmetry in the charge distribution upon application of opposite electric fields. (F) Comparing band offsets in different 2D material systems as a function of flexoelectric radius of curvature. Note: all reports curated, except for this work, are only theoretical reports (25, 29–33). (G) Comparing polarization density as a function of flexoelectric curvature. Note: all reports curated, except for this work, are only experimental reports on bulk materials (16, 23, 34, 35). All scale bars are 1  $\mu\text{m}$ .

Such an asymmetric response under bias conditions is due to the net flexoelectric-induced polarization (**Fig. 4E**); and highlights the potential for using these structures as densely packed, high-density switches, as shown in **Fig. 4D**, for advanced nanoscale electronic applications. Our observed effect represents the most pronounced flexoelectric response to date, driven by exceptionally large curvature—approaching the fundamental limits of bond lengths—and stands as the only experimental demonstration in low-dimensional material systems thus far, as shown in **Fig. 4F**. As discussed previously in Eq. 2, there is a strong inverse relationship between the radius of curvature and the flexoelectric effect. Using  $\Phi_{th} \sim 1 \text{ V}$  from **Fig. 4D**, we can describe it as the potential of a dipole as measured at proximity as follows:

$$\Phi_{th} = \frac{1}{4\pi\epsilon_0} \frac{p}{r^2} \cos \theta \quad (3)$$

where  $p$  is the dipole moment,  $r$  is the separation between the NW and scanning probe microscopy tip ( $\sim 2.52 \pm 0.27 \text{ nm}$ , as determined in a separate experiment; see **Fig. S11**), and  $\theta \sim 0$  due to normal incidence during measurement. Extracting the polarization density from eq (2) and (3) for theory and experiment yields *giant* magnitudes  $P_{th} \sim 4 \text{ C/m}^2$ ,  $P_{exp} \sim 1 \text{ C/m}^2$ . Given our curvature of  $5 \times 10^{10} \text{ m}^{-1}$ , we move towards fundamental limits for these values, as shown in **Fig. 4G**.

Our analysis further reveals that the curvature at wrinkle termini can exceed that of engineered structures by several orders of magnitude, significantly amplifying strain gradients and flexoelectric effects. The transition from flat regions to high-curvature domains provides optimal conditions for investigating the relationship between geometry and flexoelectric response, expanding insights for future device design (36). The combination of high reproducibility, scalability, and extreme curvature makes graphene nanowrinkles particularly promising for applications in energy harvesting, flexible electronics, and strain-tunable quantum devices. The ability to induce strong flexoelectric polarization without external gating suggests potential use in non-volatile memory and strain-gated transistors. Furthermore, the self-assembled nature of these wrinkles provides a cost-effective pathway for scalable flexoelectric device fabrication, which could be integrated with lab-to-fab approaches for scaling up production(37). Future work should explore integrating graphene NWs into functional electronic architectures, as well as

investigating potential coupling effects with other 2D materials<sup>(38)</sup> to engineer hybrid flexoelectric systems.

**Acknowledgments:** We thank the Rice Shared Equipment Authority (SEA) for their support.

**Funding:** SAI and PMA acknowledge and thank the Quad Fellowship. MT and ABD acknowledge the Sussex Strategy Development Fund. JGM is supported by the University of Manchester Dame Kathleen Ollerenshaw Fellowship.

**Author contributions:** SAI, VM, and MT conceived the project and designed the research. SAI, VM, and MT collected, analyzed, and presented the data and co-wrote the manuscript through the contributions of all authors. JGM performed the MD simulations. VM performed the DFT calculations. JPS collected scanning electron micrographs. MT, AD, RV, VM, and PMA acquired funding for the project. VM, PMA, AD, and MT supervised the entire project.

**Competing interests:** The authors declare that they have no competing interests.

**Data and materials availability:** Data are available in the manuscript or supplementary materials and raw data are available upon request to the authors.

## Supplementary Materials

Summary

Methods

Figs. S1 to S11

## Supplementary Information

### Sub-nm Curvature Unlocks Exceptional Inherent Flexoelectricity in Graphene

Sathvik Ajay Iyengar<sup>1</sup>, James G. McHugh<sup>2</sup>, Jonathan P. Salvage<sup>3</sup>, Robert Vajtai<sup>1</sup>, Alan Dalton<sup>4\*</sup>, Manoj Tripathi<sup>4\*</sup>, Pulickel M. Ajayan<sup>1\*</sup>, Vincent Meunier<sup>5\*</sup>

<sup>1</sup> *Department of Materials Science and NanoEngineering, Rice University; Houston, TX, 77005 USA*

<sup>2</sup> *National Graphene Institute, University of Manchester, Booth St. E., Manchester, M13 9PL, United Kingdom*

<sup>3</sup> *School of Pharmacy and Biomolecular Science, University of Brighton, Brighton BN2 4GJ, U.K*

<sup>4</sup> *Department of Physics and Astronomy, School of Mathematical and Physical Sciences, University of Sussex; Brighton BN1 9QH, United Kingdom*

<sup>5</sup> *Department of Engineering Science and Mechanics, Pennsylvania State University; University Park, PA, 16802, USA*

\*Corresponding author. Email: Alan Dalton [A.B.Dalton@sussex.ac.uk](mailto:A.B.Dalton@sussex.ac.uk), M.Tripathi@sussex.ac.uk, [ajayan@rice.edu](mailto:ajayan@rice.edu), [vincent.meunier@psu.edu](mailto:vincent.meunier@psu.edu)

#### **This file includes:**

- Methods
- Figs. S1 to S11
- References
- Supplementary movies 1-7 (attached)

#### **Methods:**

#### **Sample fabrication:**

The MoS<sub>2</sub> layer was grown via chemical vapor deposition (CVD) on a silica substrate. Comprehensive synthesis methodology can be found elsewhere (39, 40). CVD-grown graphene on Cu substrate was purchased from *Graphenea* (Spain), with added assistance related to wet transfer onto the MoS<sub>2</sub>/silica surface. The heterolayer structure was treated in an acetone bath at 40°C for 3 hours to remove PMMA residue.

#### **Raman spectroscopy:**

Raman spectroscopy is carried out by Renishaw inVia™ confocal Raman microscope with 0.8 cm<sup>-1</sup> spectral resolution. 532 nm laser (type: solid state, model: RL53250) at a power of 5 mW with 1800 mm<sup>-1</sup>

grating in 100x magnification is used. The peak position and peak intensity are then fitted by Lorentz fitting to monitor the Raman peak shift ( $\text{cm}^{-1}$ ).

### Raman-strain calculations:

Using these peak shift Strain (%) has been measured using relation (s1):

$$\begin{pmatrix} \omega_1 \\ \omega_2 \end{pmatrix} = T \begin{pmatrix} \varepsilon \\ \eta \end{pmatrix} \quad \dots (s1)$$

where,

$$T = \begin{pmatrix} -2\gamma_1\omega_1^0 & k_1 \\ -2\gamma_2\omega_2^0 & k_2 \end{pmatrix} \quad \dots (s2)$$

( $\gamma$ ) is the Grüneisen parameter, ( $K$ ) is the doping shift rate, and ( $\omega^o$ ) is the no-strain and no-doping peak position taken from the reference sample where graphene is suspended over a lithography-etched textured surface. The subscript denotes the corresponding Raman modes. As for graphene,  $\omega_1$  and  $\omega_2$  are G and 2D modes, where ( $\gamma_G$ ) = 1.95, ( $\gamma_{2D}$ ) = 3.15,  $k_G = -1.407 \times 10^{-12} \text{ cm}^{-1}$ , and  $k_{2D} = -0.285 \times 10^{-12} \text{ cm}^{-1}$  (27, 41). The vector space of Raman peak positions  $\omega_1$ - $\omega_2$  is a linear transformation from the  $\varepsilon$ - $\eta$  space, while the origin of both spaces defines the absence of strain and doping. Therefore,  $\omega$  represents the deviation of the recorded frequency from  $\omega^o$  due to strain or doping. Notably, ( $\eta$ ) represents the relative shift in the charge carrier and mostly originates from the charge exchange with the substrate. Also, the airborne impurities adsorb over the surface and at the edge region may influence ( $\eta$ ).

### Scanning probe microscopy:

Atomic Force Microscopy (AFM) characterization was carried out using a Bruker Dimension Icon with PF-QNM (PeakForce-Quantitative NanoMechanical) mode and friction mode, simultaneously measuring topography, adhesion, and friction force. Conductive AFM (C-AFM) was performed using PF-TUNA mode with a conductive probe (PFTUNA, a silicon nitride cantilever coated with Pt/Ir). The cantilever has a stiffness of 0.45 N/m. The conduction setup was established by connecting the top graphene layer to the AFM stage using conductive tape. C-AFM measurements were conducted at bias voltages ranging from -2 V to 2 V.

Kelvin Probe Force Microscopy (KPFM) was performed at room temperature using a Bruker AFM (model: ScanAsyst) with a PFQNE-AL cantilever. A single layer of CVD MoS<sub>2</sub> was used for the investigation, treated with different analytes, and its surface potential was measured. The KPFM measurement followed the two-pass technique, where the first pass scanned the sample's topography, and the second pass, conducted at a specific lift height, measured the contact potential difference (CPD, mV). A reference sample (Au-Si-Al) was used to calibrate the cantilever probe apex and determine the sample's work function (eV).

## Theory:

### Molecular Dynamics:

Molecular dynamics (MD) simulations were carried out in the LAMMPS MD environment(42). In-plane bonding of MoS<sub>2</sub> was approximated using a reactive empirical bond order potential parameterization(43), whereas graphene was simulated with the AIREBO-M potential(44). The latter adapts long-range C–C interactions to a Morse potential, fitted to quantum chemistry data, making it particularly suitable for high pressures and strains. Interlayer interactions between graphene and MoS<sub>2</sub> were approximated by Lennard-Jones 12/6 potentials for C-Mo and C-S interactions; parameters were initially taken from the Lorentz-Berthelot mixing rule(45), and were re-optimized to fit DFT-calculated interlayer adhesion. An additional, Lennard-Jones 9/3 ( $\sigma = 4 \text{ \AA}$ ,  $\epsilon = 6 \text{ meV}$ ) confining wall is applied underneath the MoS<sub>2</sub> layer, to mimic the effect of an underlying substrate. Periodic boundary conditions are applied in the in-plane directions.

Pair	$\sigma$ (Å)	$\epsilon$ (meV)
C-S	3.3	4.657
C-Mo	4.5	1.826

**Table S1:** DFT-parameterized Lennard-Jones parameters for C–S and C–Mo interactions.

Wrinkle nucleation: Finite-temperature simulations of graphene/MoS<sub>2</sub> heterostructures were performed in a periodic “ribbon” geometry, where monolayer segments of graphene and MoS<sub>2</sub> are lattice-matched along the shorter ( $y \approx 7.5 \text{ nm}$ ) direction to eliminate strain. Increasing quantities of additional graphene were then added in the long ( $x \approx 32.5 \text{ nm}$ ) direction, imposing an initial, uniform uniaxial strain ( $\epsilon_x$ ) in the graphene layer, mimicking slip and compressive strain of excess material over the MoS<sub>2</sub> surface. Hetero-bilayers were then simulated using an NVT ensemble at  $T = 100 \text{ K}$  over short,  $0.06 \text{ ns}$  timescales. Importantly, for small amounts of additional material (initial uniaxial strains of  $\epsilon_x \lesssim 0.02$ ), the graphene layer remains uniformly compressed without developing wrinkles. This behavior is consistent with the fact that spontaneous wrinkling, driven by the softening of flexural modes, only emerges once the compression exceeds a critical threshold (46). With increasing values of initial uniaxial strain, multiple, small wrinkles nucleate, and can rapidly agglomerate within the simulation time scale due to the incommensurate lattice structure and low adhesive energy of the graphene/MoS<sub>2</sub> heterointerface (see **Supplementary Movies 1-4**), which allows neighboring wrinkles to combine through mass transfer, by gliding across the MoS<sub>2</sub> surface (e.g. **Supplementary Movie 5**). Above wrinkle heights of  $\sim 2 \text{ nm}$ , adhesion between nanowrinkle walls causes it to adopt a standing collapsed structure within the simulation time scale (**Supplementary Movie 6**).

Wrinkle structure and height: Additional simulations were also performed in a larger simulation cell ( $x \approx 130 \text{ nm}$ ), to assess the dependence of wrinkle geometry on height. A representative example is shown in

**Supplementary Movie 7**, which shows the rapid growth of a collapsed wrinkle within a 0.16 ns timescale. The collapsed wrinkle reaches a free-standing height of  $h_c \approx 8$  nm, at which point it starts to bend and tilt towards the flat graphene surface, suggesting a transition to folded structures above  $h_c$ .

***Ab initio* DFT:**

Density Functional Theory (DFT) was used to calculate the relaxation of charges and the deformation of charge clouds under the influence of an electric field. We used GPAW(47, 48) with PBE(49) for the exchange-correlation potential with a Grimme correction for vdW interactions(50); 1x1x10 k-point Monkhorst-Pack grid(51), and an LCAO basis (DZP). We considered three different structures with varying ripple heights (see **Fig. S6**) The structures were relaxed until forces were all below 0.05 eV/Å. We note that PBC was not applied in the direction of the applied electric field.

Determination of flexoelectric constant: For this calculation, there is a challenge that dipole moments are not well defined in periodic systems. For this reason, we used a linear response approach where the energy  $E$  upon bending and in an external electric  $z$  field is given by:

$$E = E_0 + \mu \varepsilon_z + P \varepsilon_z^2 + O(\varepsilon_z^3) \quad \dots (s3)$$

where  $E_0$  is the energy without an electric field,  $\mu$  is the dipole moment, and  $P$  is related to the polarizability.  $\varepsilon_z$  is the static response due to bending, with  $P$  being the dynamic response to the electric field. Note that in the equation above, we limited the study to the linear case (that is: we only consider the field in one direction, perpendicular to the graphene layer) otherwise  $\mu$  would be a vector and  $P$  would be a tensor. For this calculation, we performed self-consistent DFT calculations for 33 values of the electric field from -0.15 to 0.15 V/Å. We then performed a fit for each structure and obtained the dipole and polarizations. An example of such output is shown in **Fig. S10**.

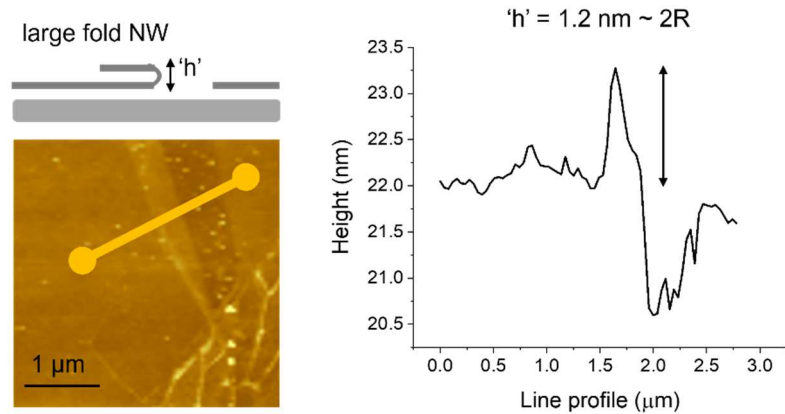


**Figure S1:** Atomic force micrograph (bottom-left) of a large fold (schematic in top-left) and corresponding height profile (right) indicates a height 'h' of roughly 1.2 nm.

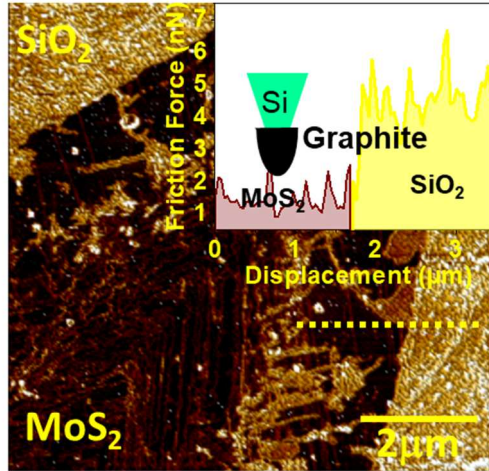


**Figure S2:** Friction force microscopy using a graphene-functionalized probe over  $\text{MoS}_2$  and silica surfaces. The color contrast represents distinguishable friction force values, with the  $\text{MoS}_2$  interface exhibiting a threefold lower friction force than silica under the same operating conditions (i.e., applied load and probe velocity).



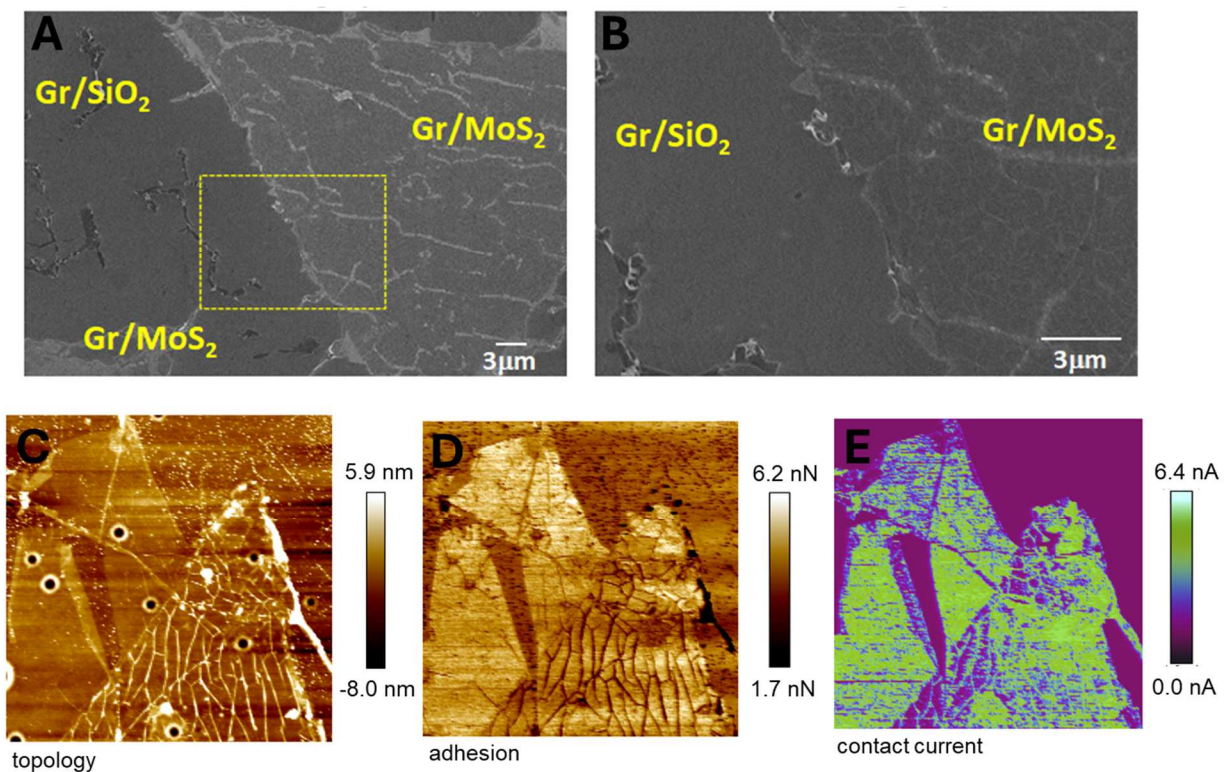


**Figure S3:** (a) SEM micrographs of graphene-covered silica and MoS<sub>2</sub> reveal a high density of graphene wrinkles on the MoS<sub>2</sub> surface. The brighter SEM contrast in wrinkled and corrugated graphene arises from variations in electron scattering trajectories, leading to higher intensity within the same area. (b) High-resolution SEM micrograph showing a relatively flat graphene surface on silica compared to the more corrugated structure on MoS<sub>2</sub>. (c) AFM topography of graphene-covered silica and MoS<sub>2</sub> supports the SEM results, confirming the higher density of graphene wrinkles on MoS<sub>2</sub>. (d) The corresponding adhesion force (pull-out) map reveals surface chemistry differences between the graphene-covered region and the bare silica substrate, showing that flat graphene exhibits higher adhesion force (nN) values toward AFM probes compared to wrinkles. (e) The conductive map of the same region, obtained under similar operating conditions, shows the current (nA) distribution across the graphene layer on silica and MoS<sub>2</sub> substrates. Notably, graphene wrinkles on MoS<sub>2</sub> exhibit higher conductivity than extended graphene layers on silica.

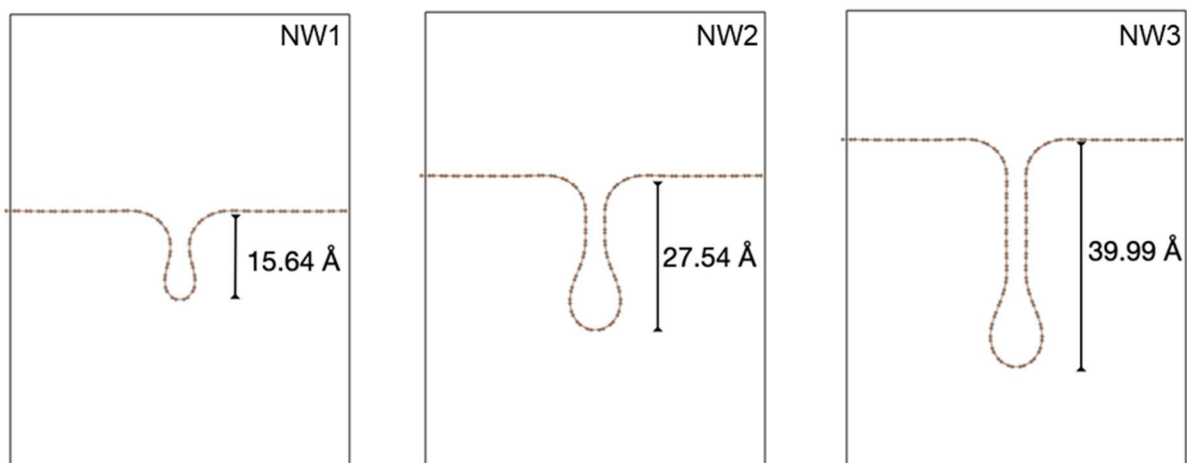


**Figure S4:** DFT relaxed structures of three wrinkle systems considered. In our main studies, the ~4 nm (NW3) wrinkle model is used. For relaxation, a flat and rigid layer was added to the top to mimic deposition on a substrate.

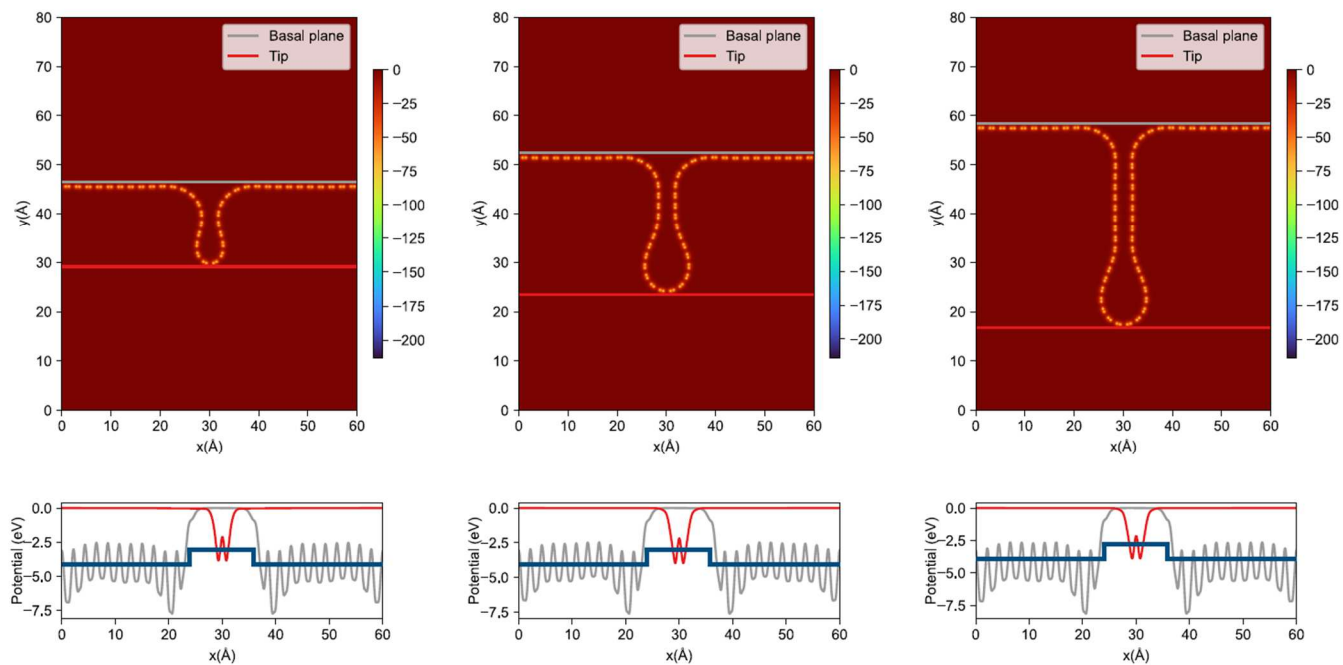


**Figure S5:** Potential in the absence of an electric field, clearly indicating the development of polarization due to the wrinkle– NW1, NW2, and NW3. In each case, this translates (bottom panel) to a potential barrier where electrons more easily escape the material due to the wrinkle. The computed band offset is about 1.2 V and does not significantly depend on the type of wrinkle.

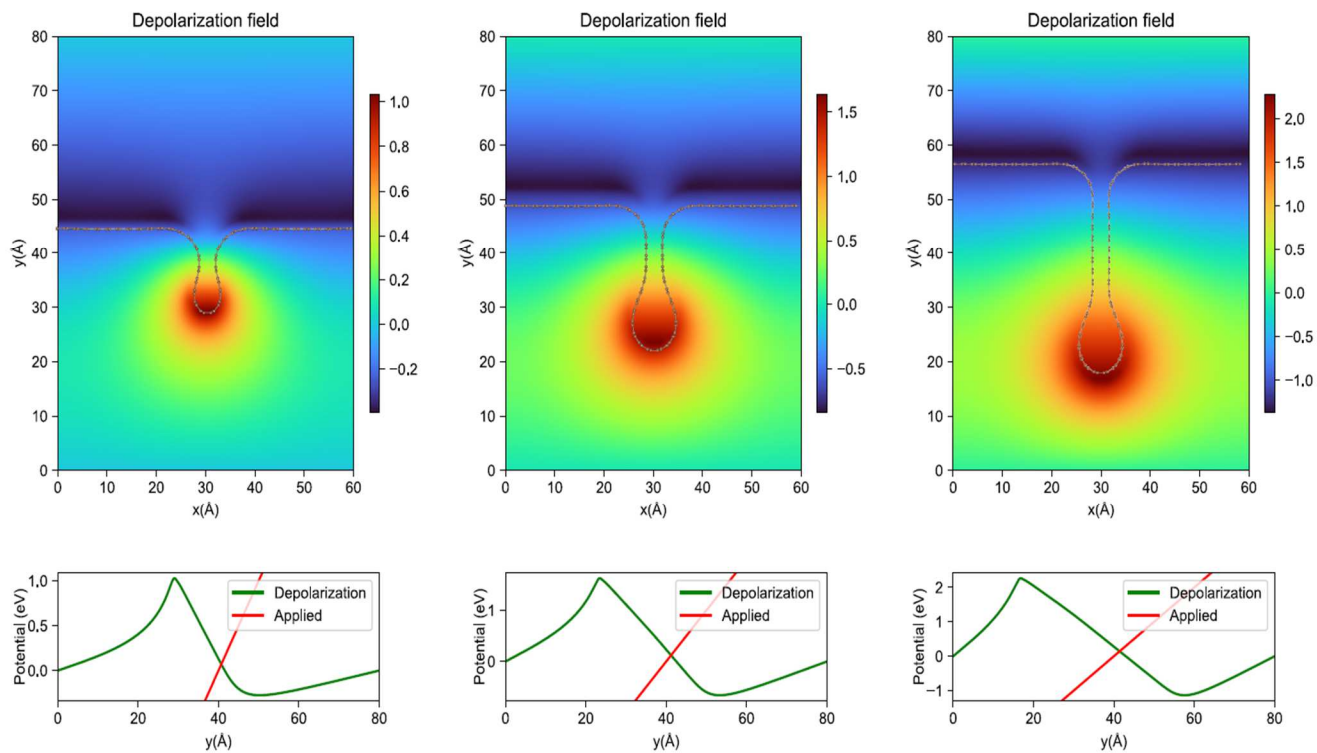


**Figure S6:** Depolarization field due to the presence of an external field shown in red in the bottom panel for NW1, NW2, and NW3.

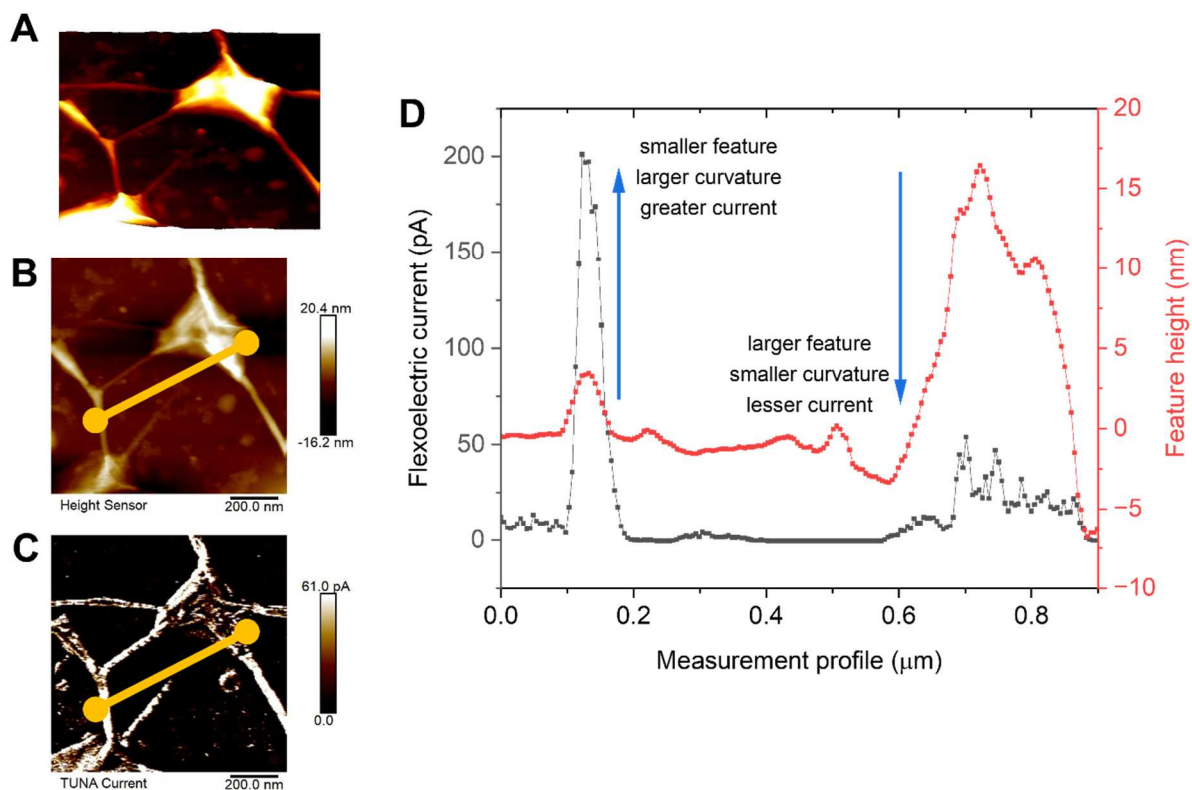


**Figure S7:** Direct comparison of the effect of curvature (and not height) on the flexoelectric current at a fixed potential. (A) 3D topology of features studied. (B) AFM micrograph. (C) C-AFM micrograph. (D) Comparing the topology and current across the drawn line profile. Note that features that do not have curvature but create variations in height (from 0.2 – 0.6 μm in the line profile along the x-axis), do not yield any current.

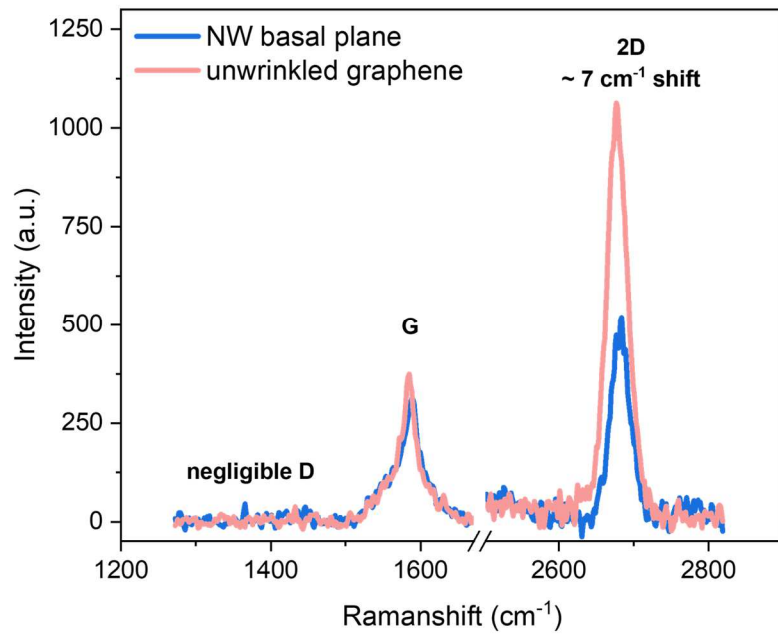


**Figure S8:** Raman spectra of graphene (D, G, and 2D) at the NW basal plane and when it is unwrinkled. There is a red shift in G peak position ( $\omega_1 = 4.9 \text{ cm}^{-1}$ ) and 2D peak position ( $\omega_1 = 7 \text{ cm}^{-1}$ ) at NW as compared to basal plane.

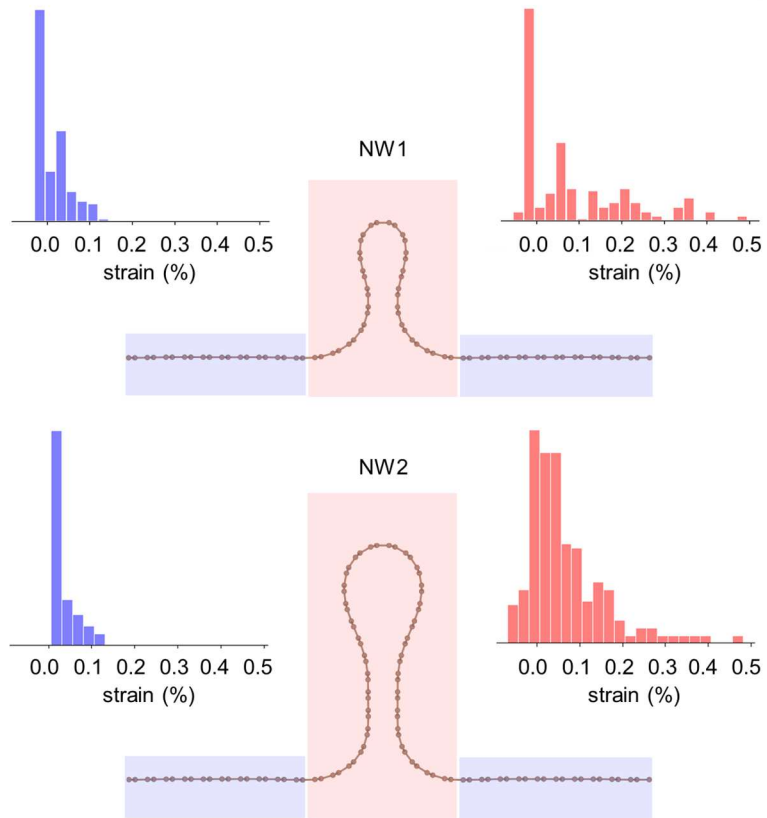


**Figure S9:** Strain lattice calculations for NW1 and NW2 (with continued NW3 in Fig. 3C).

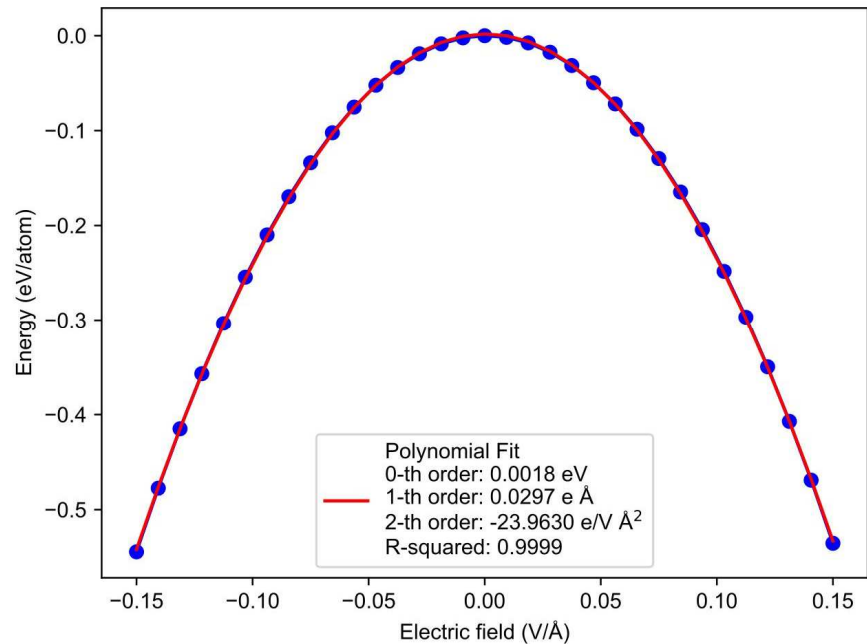


**Figure S10:** Energy as a function of applied field in the NW3 system shown in **Figure S3** (right structure). The induced dipole moment can be obtained from the fit to Equation s3.



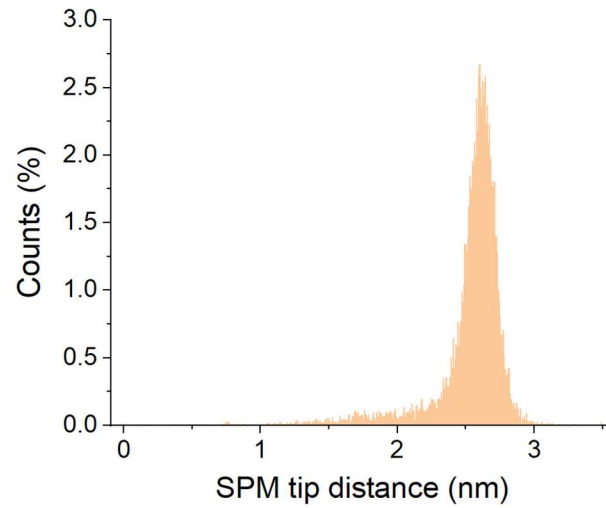


**Figure S11:** The histogram demonstrates the distribution of contact conditions, specifically the elastic deformation distance (in nanometers) associated with various wrinkles. The findings integrate the value of "jump to contact" and the minimal pressing distance to the surface, establishing a contact area between the probe apex and the NW. On a total of 512 pixels of data, the tip distance from the sample ( $d_{\text{spm-tip}}$ ) is determined to be  $2.52 \pm 0.27$  nm.

## References:

1. A. K. Tagantsev, V. Meunier, P. Sharma, Novel Electromechanical Phenomena at the Nanoscale: Phenomenological Theory and Atomistic Modeling. *MRS Bulletin* **34**, 643–647 (2009).
2. S. Krichen, P. Sharma, Flexoelectricity: A Perspective on an Unusual Electromechanical Coupling. *Journal of Applied Mechanics* **83**, 030801 (2016).
3. L. D. Marks, K. P. Olson, Flexoelectricity, Triboelectricity, and Free Interfacial Charges. *Small*, 2310546 (2024).
4. S. V. Kalinin, V. Meunier, Electronic flexoelectricity in low-dimensional systems. *Phys. Rev. B* **77**, 033403 (2008).
5. T. D. Nguyen, S. Mao, Y. Yeh, P. K. Purohit, M. C. McAlpine, Nanoscale Flexoelectricity. *Advanced Materials* **25**, 946–974 (2013).
6. P. Zubko, G. Catalan, A. K. Tagantsev, Flexoelectric Effect in Solids. *Annu. Rev. Mater. Res.* **43**, 387–421 (2013).
7. A. N. Morozovska, E. A. Eliseev, G. I. Dovbeshko, M. D. Glinchuk, Y. Kim, S. V. Kalinin, Flexoinduced ferroelectricity in low-dimensional transition metal dichalcogenides. *Phys. Rev. B* **102**, 075417 (2020).
8. M. Springolo, M. Royo, M. Stengel, Direct and Converse Flexoelectricity in Two-Dimensional Materials. *Phys. Rev. Lett.* **127**, 216801 (2021).
9. B. Wang, Y. Gu, S. Zhang, L.-Q. Chen, Flexoelectricity in solids: Progress, challenges, and perspectives. *Progress in Materials Science* **106**, 100570 (2019).
10. R. Maranganti, P. Sharma, Atomistic determination of flexoelectric properties of crystalline dielectrics. *Phys. Rev. B* **80**, 054109 (2009).
11. C. J. Brennan, R. Ghosh, K. Koul, S. K. Banerjee, N. Lu, E. T. Yu, Out-of-Plane Electromechanical Response of Monolayer Molybdenum Disulfide Measured by Piezoresponse Force Microscopy. *Nano Lett.* **17**, 5464–5471 (2017).
12. X. Wang, A. Cui, F. Chen, L. Xu, Z. Hu, K. Jiang, L. Shang, J. Chu, Probing effective out-of-plane piezoelectricity in van der Waals layered materials induced by flexoelectricity. *Small* **15**, 1903106 (2019).
13. L. Wang, S. Liu, X. Feng, C. Zhang, L. Zhu, J. Zhai, Y. Qin, Z. L. Wang, Flexoelectronics of centrosymmetric semiconductors. *Nat. Nanotechnol.* **15**, 661–667 (2020).
14. W. Peng, S. Y. Park, C. J. Roh, J. Mun, H. Ju, J. Kim, E. K. Ko, Z. Liang, S. Hahn, J. Zhang, A. M. Sanchez, D. Walker, S. Hindmarsh, L. Si, Y. J. Jo, Y. Jo, T. H. Kim, C. Kim, L. Wang, M. Kim, J. S. Lee, T. W. Noh, D. Lee, Flexoelectric polarizing and control of a ferromagnetic metal. *Nat. Phys.* **20**, 450–455 (2024).

15. S. Das, B. Wang, T. R. Paudel, S. M. Park, E. Y. Tsymbal, L.-Q. Chen, D. Lee, T. W. Noh, Enhanced flexoelectricity at reduced dimensions revealed by mechanically tunable quantum tunnelling. *Nat Commun* **10**, 537 (2019).
16. S. M. Park, B. Wang, T. Paudel, S. Y. Park, S. Das, J. R. Kim, E. K. Ko, H. G. Lee, N. Park, L. Tao, D. Suh, E. Y. Tsymbal, L.-Q. Chen, T. W. Noh, D. Lee, Colossal flexoresistance in dielectrics. *Nat Commun* **11**, 2586 (2020).
17. X. Hu, G. Yu Chen, Y. Luan, T. Tang, Y. Liang, B. Ren, L. Chen, Y. Zhao, Q. Zhang, D. Huang, X. Sun, Y. F. Cheng, J. Z. Ou, Flexoelectricity Modulated Electron Transport of 2D Indium Oxide. *Advanced Science*, 2404272 (2024).
18. J. F. Scott, Applications of Modern Ferroelectrics. *Science* **315**, 954–959 (2007).
19. K. Zheng, T. Vegge, I. E. Castelli, Giant In-Plane Flexoelectricity and Radial Polarization in Janus IV–VI Monolayers and Nanotubes. *ACS Appl. Mater. Interfaces* **16**, 19369–19378 (2024).
20. A. Lopez-Bezanilla, J. Campos-Delgado, B. G. Sumpter, D. L. Baptista, T. Hayashi, Y. A. Kim, H. Muramatsu, M. Endo, C. A. Achete, M. Terrones, V. Meunier, Geometric and Electronic Structure of Closed Graphene Edges. *J. Phys. Chem. Lett.* **3**, 2097–2102 (2012).
21. C. Lee, X. Wei, J. W. Kysar, J. Hone, Measurement of the Elastic Properties and Intrinsic Strength of Monolayer Graphene. *Science* **321**, 385–388 (2008).
22. S. Bertolazzi, J. Brivio, A. Kis, Stretching and Breaking of Ultrathin MoS<sub>2</sub>. *ACS Nano* **5**, 9703–9709 (2011).
23. P. Koirala, C. A. Mizzi, L. D. Marks, Direct Observation of Large Flexoelectric Bending at the Nanoscale in Lanthanide Scandates. *Nano Lett.* **18**, 3850–3856 (2018).
24. A. G. Petrov, Flexoelectricity of model and living membranes. *Biochimica et Biophysica Acta (BBA) - Biomembranes* **1561**, 1–25 (2002).
25. V. I. Artyukhov, S. Gupta, A. Kutana, B. I. Yakobson, Flexoelectricity and Charge Separation in Carbon Nanotubes. *Nano Lett.* **20**, 3240–3246 (2020).
26. A. A. Graf, S. P. Ogilvie, H. J. Wood, C. J. Brown, M. Tripathi, A. A. K. King, A. B. Dalton, M. J. Large, Raman Metrics for Molybdenum Disulfide and Graphene Enable Statistical Mapping of Nanosheet Populations. *Chem. Mater.* **32**, 6213–6221 (2020).
27. M. Tripathi, F. Lee, A. Michail, D. Anastopoulos, J. G. McHugh, S. P. Ogilvie, M. J. Large, A. A. Graf, P. J. Lynch, J. Parthenios, K. Papagelis, S. Roy, M. A. S. R. Saadi, M. M. Rahman, N. M. Pugno, A. A. K. King, P. M. Ajayan, A. B. Dalton, Structural Defects Modulate Electronic and Nanomechanical Properties of 2D Materials. *ACS Nano* **15**, 2520–2531 (2021).
28. E. Khestanova, F. Guinea, L. Fumagalli, A. K. Geim, I. V. Grigorieva, Universal shape and pressure inside bubbles appearing in van der Waals heterostructures. *Nat Commun* **7**, 12587 (2016).
29. J.-D. Zheng, Y.-F. Zhao, Z.-Q. Bao, Y.-H. Shen, Z. Guan, N. Zhong, F.-Y. Yue, P.-H. Xiang, C.-G. Duan, Flexoelectric effect induced p–n homojunction in monolayer GeSe. *2D Mater.* **9**, 035005 (2022).

30. H. Chen, C. Hu, L. Chen, L. Chen, K. Jiang, L. Zhu, L. Shang, Y. Li, J. Chu, S. Gong, Z. Hu, Flexoelectric effects in a bent  $\alpha$ -In<sub>2</sub>Se<sub>3</sub> ferroelectric monolayer. *Phys. Rev. B* **110**, 014102 (2024).
31. J. Dong, B. Cai, G. Ouyang, Controllable Photoelectric Properties in Double-Wall MoS<sub>2</sub> Nanotubes by the Flexoelectric Effect. *J. Phys. Chem. C* **125**, 11318–11324 (2021).
32. H. Guo, T. Yang, X. Xuan, Z. Zhang, W. Guo, Flexoelectricity in hexagonal boron nitride monolayers. *Extreme Mechanics Letters* **52**, 101669 (2022).
33. K. P. Dou, H. H. Hu, X. Wang, X. Wang, H. Jin, G.-P. Zhang, X.-Q. Shi, L. Kou, Asymmetrically flexoelectric gating effect of Janus transition-metal dichalcogenides and their sensor applications. *J. Mater. Chem. C* **8**, 11457–11467 (2020).
34. C. A. Mizzi, B. Guo, L. D. Marks, Experimental determination of flexoelectric coefficients in SrTiO<sub>3</sub>, KTaO<sub>3</sub>, TiO<sub>2</sub>, and YAlO<sub>3</sub> single crystals. *Phys. Rev. Materials* **6**, 055005 (2022).
35. X. Li, G. Ren, Y. Yun, A. S. Thind, A. K. Shah, A. Bowers, R. Mishra, X. Xu, Improper flexoelectricity in hexagonal rare-earth ferrites. *arXiv preprint arXiv:2409.17022* (2024).
36. S. A. Iyengar, A. B. Puthirath, V. Swaminathan, Realizing Quantum Technologies in Nanomaterials and Nanoscience. *Advanced Materials*, 2107839 (2022).
37. S. A. Iyengar, S. Bhattacharyya, S. Roy, N. R. Glavin, A. K. Roy, P. M. Ajayan, A Researcher's Perspective on Unconventional Lab-to-Fab for 2D Semiconductor Devices. *ACS Nano* **17**, 12955–12970 (2023).
38. P. Kumar, G. Singh, X. Guan, S. Roy, J. Lee, I. Y. Kim, X. Li, F. Bu, R. Bahadur, S. A. Iyengar, J. Yi, D. Zhao, P. M. Ajayan, A. Vinu, The Rise of Xene Hybrids. *Advanced Materials* **36**, 2403881 (2024).
39. X. Wang, Y. Gong, G. Shi, W. L. Chow, K. Keyshar, G. Ye, R. Vajtai, J. Lou, Z. Liu, E. Ringe, B. K. Tay, P. M. Ajayan, Chemical Vapor Deposition Growth of Crystalline Monolayer MoSe<sub>2</sub>. *ACS Nano* **8**, 5125–5131 (2014).
40. L. M. Sassi, S. A. Iyengar, A. B. Puthirath, Y. Huang, X. Li, T. Terlier, A. Mojiypour, A. P. C. Teixeira, P. Bharadwaj, C. S. Tiwary, others, Bottom-up Integration of TMDCs with Pre-Patterned Device Architectures via Transfer-free Chemical Vapor Deposition. *arXiv preprint arXiv:2305.14554* (2023).
41. N. Ferralis, Probing mechanical properties of graphene with Raman spectroscopy. *J Mater Sci* **45**, 5135–5149 (2010).
42. A. P. Thompson, H. M. Aktulga, R. Berger, D. S. Bolintineanu, W. M. Brown, P. S. Crozier, P. J. In 't Veld, A. Kohlmeyer, S. G. Moore, T. D. Nguyen, R. Shan, M. J. Stevens, J. Tranchida, C. Trott, S. J. Plimpton, LAMMPS - a flexible simulation tool for particle-based materials modeling at the atomic, meso, and continuum scales. *Computer Physics Communications* **271**, 108171 (2022).
43. T. Liang, S. R. Phillpot, S. B. Sinnott, Parametrization of a reactive many-body potential for Mo–S systems. *Phys. Rev. B* **79**, 245110 (2009).

44. T. C. O'Connor, J. Andzelm, M. O. Robbins, AIREBO-M: A reactive model for hydrocarbons at extreme pressures. *The Journal of Chemical Physics* **142**, 024903 (2015).
45. M. R. Vazirisereshk, H. Ye, Z. Ye, A. Otero-de-la-Roza, M.-Q. Zhao, Z. Gao, A. T. C. Johnson, E. R. Johnson, R. W. Carpick, A. Martini, Origin of Nanoscale Friction Contrast between Supported Graphene, MoS<sub>2</sub>, and a Graphene/MoS<sub>2</sub> Heterostructure. *Nano Lett.* **19**, 5496–5505 (2019).
46. P. L. De Andres, F. Guinea, M. I. Katsnelson, Bending modes, anharmonic effects, and thermal expansion coefficient in single-layer and multilayer graphene. *Phys. Rev. B* **86**, 144103 (2012).
47. J. Enkovaara, C. Rostgaard, J. J. Mortensen, J. Chen, M. Duřak, L. Ferrighi, J. Gavnholt, C. Glinsvad, V. Haikola, H. A. Hansen, H. H. Kristoffersen, M. Kuisma, A. H. Larsen, L. Lehtovaara, M. Ljungberg, O. Lopez-Acevedo, P. G. Moses, J. Ojanen, T. Olsen, V. Petzold, N. A. Romero, J. Stausholm-Møller, M. Strange, G. A. Tritsarlis, M. Vanin, M. Walter, B. Hammer, H. Häkkinen, G. K. H. Madsen, R. M. Nieminen, J. K. Nørskov, M. Puska, T. T. Rantala, J. Schiøtz, K. S. Thygesen, K. W. Jacobsen, Electronic structure calculations with GPAW: a real-space implementation of the projector augmented-wave method. *J. Phys.: Condens. Matter* **22**, 253202 (2010).
48. J. J. Mortensen, L. B. Hansen, K. W. Jacobsen, Real-space grid implementation of the projector augmented wave method. *Phys. Rev. B* **71**, 035109 (2005).
49. J. P. Perdew, K. Burke, M. Ernzerhof, Generalized Gradient Approximation Made Simple. *Phys. Rev. Lett.* **77**, 3865–3868 (1996).
50. E. Caldeweyher, C. Bannwarth, S. Grimme, Extension of the D3 dispersion coefficient model. *The Journal of Chemical Physics* **147**, 034112 (2017).
51. H. J. Monkhorst, J. D. Pack, Special points for Brillouin-zone integrations. *Phys. Rev. B* **13**, 5188–5192 (1976).